AN INVESTIGATION OF MARFE INDUCED H-L BACK TRANSITIONS

A Thesis

Presented to

The Academic Faculty

By

Zachary W. Friis

In Partial Fulfillment

of the Requirements for the Degree

Master of Science in Nuclear Engineering

Georgia Institute of Technology

December 2005

AN INVESTIGATION OF MARFE INDUCED H-L BACK TRANSITIONS

Approved by:

Dr. Weston M. Stacey, Advisor
School of Nuclear and Radiological Engineering
Georgia Institute of Technology

Dr. John Mandrekas
School of Nuclear and Radiological Engineering
Georgia Institute of Technology

Dr. Cassiano de Oliveira
School of Nuclear and Radiological Engineering
Georgia Institute of Technology

Date Approved: September 8, 2005

ACKNOWLEDGMENTS

I would like to express my gratitude to Dr. Stacey for suggesting the topic, allowing me the use of his analysis codes, and giving abundant advice. I would also like to thank Drs. T. W. Petrie and A. W. Leonard of General Atomics and the members of the DIII-D National Team who contributed to the measurement and reduction of the data used in this work and to the running of the DIII-D facility.

This work was performed under U.S. Dept. of Energy Grant DE-FG02-99ER54538 with the Georgia Tech Research Corporation and Contract DE-AC03—99ER54463 with General Atomics Company.

TABLE OF CONTENTS

LIST OF TABLES

LIST OF FIGURES

SUMMARY

The common observation that the onset of a core MARFE (edge localized, poloidally asymmetric, highly radiating region) is followed immediately by a High-to-Low (H-L) confinement mode transition in DIII-D was investigated by comparing a theoretical prediction of the threshold non-radiative power across the separatrix (surface defining the confined plasma region) needed to maintain H-mode with an experimental determination of the non-radiative power flowing across the separatrix. It was found in three shots with continuous gas fueling that the increased neutral influx associated with the MARFE formation caused a sharp increase in the predicted threshold non-radiative power crossing the separatrix that was required for the plasma to remain in H-mode to a value comparable to the experimental power crossing the separatrix, indicating a theoretical prediction of a H-L transition in agreement with experimental observation.

CHAPTER 1 INTRODUCTION

During the past fifty years, the quest for terrestrial fusion has advanced so much that many plasma physicists agree it is no longer a question of time, but a question of money, before a Q (ratio of fusion energy to input power) of greater than ten is achieved, at which point the feasibility of a fusion power reactor would be realized. One of the most promising discoveries in the field of magnetically confined plasmas has been the observation of a high confinement regime (H-mode). H-mode means the time that heating energy remains in the plasma is large, or high, relative to the often-observed low confinement regime (L-mode) for which this time is short, or low.

It was discovered that the plasma transitioned to this H-mode from L-mode once the non-radiative power flux through the separatrix exceeded a certain threshold value. This power threshold was observed in several Tokamaks, and an empirical correlation was formulated [1]:

$$P_{LH}^{(MW)} = (2.84/A_i)\bar{n}_{20}^{0.58} B^{0.82} Ra^{0.81} \quad (1)$$

where R(m) and a(m) are the major and minor radii, respectively, A_i(amu) is the plasma ion mass, $\bar{n}_{20}$ $(10^{20}\ \mathrm{m}^{-3})$ is

the plasma line-average electron density, and B(T) is the toroidal magnetic field. Of these parameters, the line-average electron density is the only one that reflects changes in the plasma properties as the discharge evolves.

In the DIII-D tokamak, researchers observed [2] that when there was an attempt to build up the density of an H-mode plasma by injecting gas, a dense, cool, poloidally asymmetric, highly radiating region (MARFE) formed in the plasma edge. Immediately following MARFE formation the plasma confinement would transition from H-mode to L-mode. The purpose of this thesis is to investigate the role MARFEs have in the H-L transition. It is important to understand this relation because H-mode is important to using magnetically confined plasmas as a viable energy source.

CHAPTER 2 BACKGROUND

2.1 WHAT ARE MARFEs?

In the early eighties, researchers working at the DIII, FT, ASDEX, and PDX facilities made initial observations of region formations in the plasma that were poloidally localized, but toroidally symmetric. The regions were cool, dense, and formed near the divertor[a] [4,5,6]. These regions also formed at density levels just below the density limit at which the plasma would lose total confinement (or disrupt). Early on, researchers predicted that density levels at which this phenomena occurred could cause a drop in the ionization energy of the recycling neutrals in the edge. The end result of this drop would be a decrease in heat flux through the edge, due to increased radiation, which caused the layer just outside the separatrix to become unstable [7–10]. Researchers at Alcator C had similar experiences [11]. However, the Alcator group observed a larger degree of heat flux loss, but attributed the additional loss to low-Z impurity radiation. Eventually, the name “multifaceted asymmetric

[a] Similar observations have been made in limiter Tokamaks and stellarators [3]; however, this thesis is only concerned with research done on diverted Tokamaks.

radiation from the edge", or MARFE, was given to this cool, dense, and radiating region. This region was found to have radiated a significant portion of the input power.

Drake later suggested that MARFEs form as an effect of radiative condensation [12]. This explanation was not without an astrophysical precedent [13,14]. In this explanation, a local increase in plasma density increases the radiation rate. This reduces the local temperature, which requires the density flowing along field lines to further increase in the cool region ("condense") in order to maintain constant pressure across the field lines. Later refined, this explanation included a density variation in the edge and the radiation effects of ionizing neutrals, as well as temperature gradient boundary conditions in the edge [15-17].

Eventually, Georgia Tech researchers expanded upon these explanations and developed a more precise model for when the plasma first detaches from the divertor (we will refer to this as the divertor MARFE). They also developed a model for when the divertor MARFE crosses the separatrix (or X-point MARFE). Chapter 6 of this work includes a more detailed discussion of these two models.

It should be noted that a divertor MARFE can often be stabilized in Tokamaks by terminating the external density

source (gas fueling, pumping, puffing, etc.) However, if the divertor MARFE continues to be fueled, an X-point MARFE will occur. When this happens, the plasma will most certainly lose good confinement. There are numerous cases of this happening.

2.2 MARFEs FOLLOWED BY H-L TRANSITION

Researchers at DIII-D have carried out many density limit experiments. They often looked for the maximum density achieved before the plasma destroyed itself (or disrupted). Many different modes of operation have been carried out during these experiments. Of particular interest to us are the discharges in which ELMing H-mode plasmas were used. ELMing H-mode plasmas are plasmas that have not suppressed the Edge Localized Mode MHD instabilities (ELMs) [2].

In many of these H-mode shots, it was observed that the plasma did not disrupt, but transitioned back to L-mode. In many cases, they observed a density build up near the X-point of the divertor and a drop in the edge electron temperature profile. Accompanying this, a large percentage

of input power was radiated from near the divertor/X point region [2].

The H-L transition would also occur in a number of radiative divertor experiments in which D_2 was injected into an ELMing H-mode plasma [18]. In these experiments, researchers observed the plasma partially detach from the wall of the chamber. Accompanying this was a collapse of $T_{e,sep}$, as well as a buildup of density upstream of the outboard divertor separatrix strike point (divertor MARFE). As D_2 continued to be injected, the divertor MARFE worked its way up from the strike point to the X-point (also known as core MARFE).

Following the X-point MARFE, the H-mode plasma would transition back to L-mode [18]. Numerous cases of similar incidences have taken place in the DIII-D facility. So many incidences have occurred that it has been suggested that MARFEs may in fact be the cause for the transition from H to L mode in many of these discharges [19]. However, DIII-D is not the only machine to have observed such phenomena.

Researchers at the ASDEX-Upgrade facility often observed the same phenomena in many density limit experiments while operating in H-mode. The ASDEX-Upgrade team found that the H-L transition was related to a decreased edge temperature gradient that developed in

parallel with an increasing degree of detachment [20]. Similarly, in JET with the MARK I divertor, many experiments were carried out in which the plasma was partially detached. In these experiments, the plasma was brought to H-mode until a certain density limit was reached. After this point, the plasma would fully detach and an X-point MARFE would occur. Immediately after the X-point MARFE, the plasma would lose confinement and slip back into L-mode [21]. Researchers at JT-60U have also experienced a similar phenomenon. Experiments were conducted in discharges with the ion grad-B drift directed towards the divertor. In these discharges, a radiative region gradually carried heat flux away from the divertor strike plates until a core MARFE formed. In JT-60U the core MARFE would eventually cause disruption (complete loss of confinement) [22].

As one can see, we are not the first to study the phenomena of MARFEs or their affects. In the remainder of this work, we will be concentrating our efforts on why X-point MARFEs cause loss of confinement. To do this we will need to look at a few analytical tools used in our analysis and at the diagnostics used to determine the MARFE onset, the H-L transition, and other parameters that are needed to evaluate the theoretical predictions.

CHAPTER 3 MODEL FOR L–H TRANSITIONS

While Eq.(1) is useful for estimates, the empirical correlation is based on machine parameters. These machine parameters remain largely unchanged as the plasma transitions from H-mode to L-mode, yet something must be changing for a transition to occur. Since the MARFE starts out in the edge, it is likely that the cause for the transition occurs in the edge. For this reason, we will use a recently developed theoretical model for the L–H transition. This model came about by researchers at the Georgia Institute of Technology in conjunction with researchers at the DIII-D facility who were investigating two-dimensional thermal instabilities in the plasma edge that could be driven by edge impurity and atomic physics cooling and suppressed by large edge temperature gradients [23].

To develop this model, researchers started by performing a linear analysis of the edge transport barrier. They considered two-dimensional perturbations in the plane $(r,\perp)$ perpendicular to the magnetic field and then considered the effect of coupled $v_\perp, v_r$ and density perturbations on the temperature perturbations (here r denotes the radial direction, and $\perp$ denotes the direction

perpendicular both to r and the magnetic field). Their general formalism also included conductive and convective heat transport. To start with, a set of balance equations were considered. The first being the ion particle balance [23].

$$\frac{\partial n}{\partial t}+\frac{\partial}{\partial r}(n\upsilon_{ir})+\frac{\partial}{\partial 1_{\perp}}(n\upsilon_{i\perp})=n\upsilon_{ion} \tag{2}$$

The electron particle balance looks the same, but involves the electron density ($1_{\perp}$ denotes the direction perpendicular to r and the magnetic field). The next balance equation considered was the ion radial momentum balance [23].

$$m_i\frac{\partial(n\upsilon_{ir})}{\partial t}+\frac{\partial(nT_i)}{\partial r}-neE_r-ne\upsilon_{i\perp}B=nm_iv_{ie}(\upsilon_{er}-\upsilon_{ir})-nm_i\upsilon_{ir}v_{at} \tag{3}$$

and the ion perpendicular momentum balance equation is

$$m_i\frac{\partial(n\upsilon_{i\perp})}{\partial t}+\frac{\partial(nT_i)}{\partial 1_{\perp}}-neE_{\perp}-ne\upsilon_{ir}B=nm_iv_{ie}(\upsilon_{e\perp}-\upsilon_{i\perp})-nm_i\upsilon_{i\perp}v_{at} \tag{4}$$

where v_{ie} in both is the ion-electron collision frequency. The electron radial and perpendicular momentum balance equations followed the same as the above (respectively)

except, there was a $-e$ in the third term. Additionally there is no v_{at} term in either.

For the purposes of our research will only consider the case of weak temperature equilibrium for the energy balance equations. The Georgia Tech researchers looked at the strong temperature equilibrium case; however, for the region that we will be examining the weak temperature equilibrium case is more realistic.

Continuing with the derivation of the model, the researchers next considered two separate energy balance equations for the ions and electrons. For the ions they used [23]

$$\frac{3}{2}\frac{\partial(nT_i)}{\partial t}-\frac{\partial}{\partial r}\left(n\chi_{ri}\frac{\partial T_i}{\partial r}\right)-\frac{\partial}{\partial 1_\perp}\left(n\chi_{\perp i}\frac{\partial T_i}{\partial 1_\perp}\right)+\frac{5}{2}\frac{\partial(nT_i\upsilon_{ir})}{\partial r}+\frac{5}{2}\frac{\partial(nT_i\upsilon_{i\perp})}{\partial 1_\perp}=H_i-\frac{3}{2}nT_iv_{at} \tag{5}$$

and for the electrons

$$\frac{3}{2}\frac{\partial(nT_e)}{\partial t}-\frac{\partial}{\partial r}\left(n\chi_{re}\frac{\partial T_e}{\partial r}\right)-\frac{\partial}{\partial 1_\perp}\left(n\chi_{\perp e}\frac{\partial T_e}{\partial 1_\perp}\right)+\frac{5}{2}\frac{\partial(nT_e\upsilon_{er})}{\partial r}+\frac{5}{2}\frac{\partial(nT_e\upsilon_{e\perp})}{\partial 1_\perp}=H_e-nn_zL_z-nE_{ion}v_{ion} \tag{6}$$

They found the equilibrium solution to Eq.(2), which gave a relationship between the radial density and velocity gradients and the ionization frequency [23]

$$L_{\upsilon}^{-1} = -\left(L_n^{-1} + \frac{v_{ion}}{\upsilon_r} \right) - (\Delta_{\upsilon}^{-1} + \Delta_{\upsilon}^{-1}) \frac{\upsilon_{i\perp}}{\upsilon_{ir}} \simeq -\left(L_n^{-1} + \frac{v_{ion}}{\upsilon_r} \right) \tag{7}$$

where they have assumed that the perpendicular gradients, $\Delta_n^{-1} \equiv -1/n\partial n/\partial 1_{\perp}$, etc., are small compared to radial gradients in the plasma edge [23].

The equilibrium solution to the ion and electron radial momentum balance yielded expressions for the equilibrium perpendicular velocities [23].

$$\begin{aligned} \bar{\upsilon}_{i\perp} &= \frac{-eE_r + T_i(L_n^{-1} + L_{T_i}^{-1})}{eB} \\ \bar{\upsilon}_{e\perp} &= \frac{-eE_r + T_e(L_n^{-1} + L_{T_e}^{-1})}{eB} \end{aligned} \tag{8}$$

Equilibrium solutions to Eq.(4) were found for the ions and electrons, then added and subtracted to obtain

$$\begin{aligned} E_{\perp} = \upsilon_r B - \frac{T_e}{e(T_e + T_i)} \\ \times \left(\frac{v_{at}}{\Omega_i} \left(eE_r + T\left(L_n^{-1} + L_{T_i}^{-1} \right) + \frac{v_{ie}}{\Omega_i} \left(1 + \frac{v_{ei}}{v_{ie}} \frac{c_{si}^2}{c_{se}^2} \right) \times L_n^{-1} \left(T_e + T_i \right) + T_e L_{T_e}^{-1} + T_i L_{T_i}^{-1} \right) \right) \end{aligned} \tag{9}$$

where $\Omega_i \equiv eB/m_i$ is the ion gyrofrequency.

The equilibrium solutions to Eq.(5) and Eq.(6) followed as such respectively for the ions

$$\begin{aligned} &-\overline{\chi}_{ir}\left(\left(\frac{1}{T}\frac{\partial^2 T_i}{\partial r^2}\right)+L_{Ti}^{-1}\left(L_n^{-1}+vL_{Ti}^{-1}\right)\right)-\overline{\chi}_{i\perp}\left(\left(\frac{1}{T_i}\frac{\partial^2 T_i}{\partial 1_\perp^{\,2}}\right)+\Delta_{Ti}^{-1}\left(\Delta_n^{-1}+v\Delta_{Ti}^{-1}\right)\right) \\ &=\frac{5}{2}\overline{\upsilon}_{ir}\left(L_n^{-1}+L_{Ti}^{-1}+L_\upsilon^{-1}\right)+\frac{5}{2}\overline{\upsilon}_{i\perp}\left(\Delta_n^{-1}+\Delta_{Ti}^{-1}+\Delta_{\upsilon i}^{-1}\right)+\frac{\overline{H}_i}{nT_i}-\frac{3}{2}\overline{v}_{at} \end{aligned} \tag{10}$$

and electrons.

$$\begin{aligned} &-\overline{\chi}_{er}\left(\left(\frac{1}{T}\frac{\partial^2 T_e}{\partial r^2}\right)+L_{Te}^{-1}\left(L_n^{-1}+vL_{Te}^{-1}\right)\right)-\overline{\chi}_{e\perp}\left(\left(\frac{1}{T_e}\frac{\partial^2 T_e}{\partial 1_\perp^{\,2}}\right)+\Delta_{Te}^{-1}\left(\Delta_n^{-1}+v\Delta_{Te}^{-1}\right)\right) \\ &=\frac{5}{2}\overline{\upsilon}_{er}\left(L_n^{-1}+L_{Te}^{-1}+L_\upsilon^{-1}\right)+\frac{5}{2}\overline{\upsilon}_{e\perp}\left(\Delta_n^{-1}+\Delta_{Te}^{-1}+\Delta_{\upsilon e}^{-1}\right)+\left(\frac{\overline{H}_e}{nT_e}-\frac{\overline{n}_z\overline{L}_z}{T_e}-\frac{E_{ion}}{T_e\overline{v}_{ion}}\right) \end{aligned} \tag{11}$$

Other physical restraints were imposed on the equilibrium solution [23]. Charge neutrality required that $n_i = n_e \equiv n$, therefore $L_{ni}^{-1} = L_{ne}^{-1} \equiv L_n^{-1}$. Likewise, ambipolarity required $\upsilon_{ir} = \upsilon_{er} \equiv \upsilon_r$, which required $L_{\upsilon i}^{-1} = L_{\upsilon e}^{-1} \equiv L_\upsilon^{-1}$. The current also had to be satisfied.

$$0 = \nabla \bullet \boldsymbol{j} = \frac{\partial}{\partial r}\left(n_i\upsilon_{ir} - n_e\upsilon_{er}\right)+\frac{\partial}{\partial 1_\perp}\left(n_i\upsilon_{i\perp} - n_e\upsilon_{e\perp}\right) \tag{12}$$

If the researchers took into account the charge neutrality and ambipolarity, the current required $\upsilon_{i\perp}(\Delta_{ni}^{-1}+\Delta_{vi}^{-1}) = -\upsilon_{e\perp}(\Delta_{ne}^{-1}+\Delta_{ve}^{-1})$.

In general, $(\Delta_{ni}^{-1}+\Delta_{vi}^{-1})=(\Delta_{ne}^{-1}+\Delta_{ve}^{-1})=0$ was also required in order to satisfy Eq.(12) [23].

After obtaining the equilibrium solutions and imposed physical constraints, the researchers continued their analysis by considering a two-dimensional $(r,\perp)$ perturbation about the equilibrium solutions. The perturbation took the form

$$x'(r,l_\perp,t)=x(r,l_\perp)+\tilde{x}\sin\left(\frac{\pi r}{\Delta_{TB}}\right)\sin\left(\frac{\pi l_\perp}{L_\perp}\right)e^{\omega t} \tag{13}$$

where they omitted the over bar used to denote equilibrium. Δ_{TB} was defined as the thickness of the transport barrier inside the separatrix. This was used because for their analysis, they were only concerned with instabilities localized inside the transport barrier. ω was the growth rate of greatest interest for us, because as we will now see, it leads to a new expression for Eq.(1).

The Georgia Tech researchers used Eq.(13) to expand the ion density, velocities and temperature in Eq.(5). The results were then linearized. Next they used the previous equilibrium constraints on the ion distributions and found a solution for the growth rate of the thermal instability mode associated with ion temperature perturbations in the weak equilibrium limit.

$$\omega_i = -\frac{1}{3}[2\chi_{ir}\left(\left(\frac{\pi}{\Delta_{TB}}\right)^2 + vL_{T_i}^2\right) + 2\chi_{i\perp}\left(\left(\frac{\pi}{L_\perp}\right)^2 + v\Delta_{Ti}^{-1}\right) + 5\upsilon_r vL_{Ti}^{-1} + 5\upsilon_{i\perp}v\Delta_{Ti}^{-1}$$
$$-5(v-1)v_{ion} - 3v_{at}\times\left(v - \left(1 + \frac{T_i}{v_{at}}\frac{\partial v_{at}}{\partial T_i}\right)\right) - 5\rho_i c_{si}(L_n^{-1}\Delta_{T_i}^{-1} - L_{T_i}^{-1}\Delta_n^{-1}) + \frac{2}{n}\left(v\frac{H_i}{T_i} - \frac{\partial H_i}{\partial T_i}\right)] \quad (14)$$

The same thing was done with Eq.(6) to find a solution for the growth rate of the thermal instability mode associated with electron temperature perturbations in the weak equilibrium limit [23].

$$\omega_e = -\frac{1}{3}[2\chi_{er}\left(\left(\frac{\pi}{\Delta_{TB}}\right)^2 + vL_e^{-2}\right) + 2\chi_{e\perp}\left(\left(\frac{\pi}{L_\perp}\right)^2 + v\Delta_{Te}^{-2}\right) + 5v\upsilon_r L_{Te}^{-1}$$
$$+5\upsilon_{e\perp}v\Delta_{Te}^{-1} - 2n_z\left(v\frac{L_z}{T_e} - \frac{\partial L_z}{\partial T_e}\right) - v_{ion}\left(5(v-1) - 3\frac{T_e}{v_{ion}}\frac{\partial v_{ion}}{\partial T_e}\right) \quad (15)$$
$$-2v_{ion}\frac{E_{ion}}{T_e}\left(v - \frac{T_e}{v_{ion}}\frac{\partial v_{ion}}{\partial T_e}\right) + 5\rho_e c_{se}\left(L_{T_e}^{-1}\Delta_n^{-1} - \Delta_{T_e}^{-1}L_n^{-1}\right) + \frac{2}{n}\left(v\frac{H_e}{T_e}\frac{\partial H_e}{\partial T_e}\right)]$$

The researchers then generalized Eq.(14) and Eq.(15) to obtain

$$\omega = -\frac{2}{3}\left(\chi\left(vL_T^{-2} + k_r^2\right) + \frac{5}{2}vL_T^{-1} - \alpha\right) \quad (16)$$

Where for the ions α equals

$$\alpha_i = \frac{5}{2}(v-1)\nu_{ion} + \frac{3}{2}\nu_{at}^c\left(v - \left[1 + \frac{T_i}{\nu_{at}^c}\frac{\partial \nu_{at}^c}{\partial T_i}\right]\right) - \frac{1}{n}\left(v\frac{H_i}{T_i} - \frac{\partial H_i}{\partial T}\right) \quad (17)$$

and for the electrons.

$$\alpha_e = n_z\left(\frac{\nu L_z}{T_e} - \frac{\partial L_z}{\partial T_e}\right) + \nu_{ion}\left\{\frac{5}{2}(\nu-1) + \nu\frac{E_{ion}}{T_e} - \left(\frac{3}{2} + \frac{E_{ion}}{T_e}\right)\frac{T_e}{\nu_{ion}}\frac{\partial \nu_{ion}}{\partial T_e}\right\} - \frac{1}{n}\left(\nu\frac{H_e}{T_e} - \frac{\partial H_e}{\partial T_e}\right) \quad (18)$$

The first two terms of Eq.(16) are the stabilizing heat conduction and convection. The α terms form the destabilizing atomic physics (which include impurity radiation) cooling terms and the stabilizing effect of heating that may be present in the plasma edge [24].

In Eq.(16), χ was the radial thermal diffusivity, and was proportional to T^{ν}. Many anomalous transport theories [25] suggested 3/2 < ν < 7/2. $L_T^{-1} = -(dT/dr)/T$, $\Gamma_\perp$ was the average radial particle flux flowing outward through the plasma edge region, ν_{ion} was the neutral ionization frequency, and ν_{at}^{c} was the frequency of charge-exchange plus elastic scattering reactions with "cold" neutrals. E_{ion} was the ionization energy, n_z and L_z were the density and radiation emissivity of impurity ions, and H was any external heating. As followed from their derivation, all quantities were in the plasma edge [24].

A few important consequences followed from equation 16 [24]. The ion instability growth rate becomes more positive (or less negative) if the ion temperature gradient scale

length increases or if the neutral density increases. In a similar fashion the electron instability growth rate becomes more positive (or less negative) as the edge neutral and impurity densities and emissivities and the electron temperature gradient scale length increases. Also, both ω_i and ω_e become more positive (or less negative) with decreasing edge density or temperature and increasing non-radiative heat flux through the edge of the respective species since $q_\perp = nT\chi L_T^{-1}$ [24].

During the remainder of their analysis, researchers worked only with the general form of Eq.(16) for simplicity. However, it should be noted that they made it clear that the end result of their analysis was actually two separate equations for the electrons and ions.

Frequently [24], a simple estimate for the incremental transport associated with instabilities with a growth rate of ω and de-correlation length δ is given by $\Delta\chi \approx \omega\delta^2$. As aforementioned, they were only considering thermal instabilities in the transport barrier (instabilities with a radial wavelength k_r^{-1}), thus they took $\delta \approx k_r^{-1}$. From this, they wrote the thermal diffusivity for ions and electrons in the edge as the sum of a background transport term, χ^0, and a thermal instability term $C_\chi \omega k_r^{-2}$

$$\chi = \chi^0 + C_\chi \omega k_r^{-2} H(\omega > 0), \tag{19}$$

where C_χ is an order of unity constant and H is the Heaviside function, which vanishes when $\omega \leq 0$ and is unity when ω > 0.

The researchers then used the standard form for the thermal conduction. When this was used, a relation between the average ion and electron temperature gradients in the edge to the corresponding heat diffusivities and average power flux, $Q_\perp$, and convective particle flux, $\Gamma_\perp$, through the edge could be found [24].

$$G_\perp \equiv \left(\frac{Q_\perp}{nT} - \frac{5}{2} \frac{\Gamma_\perp}{n} \right) = \chi L_T^{-1} \tag{20}$$

The researchers noted that these average values of $Q_\perp$ and $\Gamma_\perp$ in an edge region extending a distance Δ inward from the separatrix differ from the values of these quantities crossing the separatrix because of the atomic physics cooling and ionization particle sources [26].

$$\Gamma_\perp = \Gamma_\perp^{sep} - \frac{1}{2} n \nu_{ion} \Delta \tag{21}$$

$$Q_{\perp e} = Q_{\perp e}^{sep} + \frac{1}{2} n T_e \left(\frac{n_z L_z}{T_e} + \frac{3}{2} \nu_{ion} \right) \Delta \tag{22}$$

$$Qi = Q_{\perp i}^{sep} + \frac{1}{2} n T_i \frac{3}{2} \nu_{at}^{c} \Delta \tag{23}$$

Proceeding with their analysis, they assumed that if the thermal instabilities in the edge are zero, then $\chi = \chi^0$. This was used to solve Eq.(16) for the threshold value of the average temperature gradient scale length in the edge for which thermal instabilities are suppressed [24].

$$(L_T^{-1})_{thresh} = \frac{(\frac{5}{4}\frac{\Gamma_\perp}{n})}{\chi^0} \left[\sqrt{1 + \frac{\left(\chi^0 \left(\alpha - \chi^0 k_r^2\right)/\nu\right)}{\left(\frac{5}{4}\frac{\Gamma_\perp}{n}\right)^2}} - 1 \right] \tag{24}$$

Next, they used Eq.(20) in Eq.(24) to find a threshold value for the average non-radiative power flux through the edge for which thermal instabilities are suppressed [24].

$$\left(\frac{Q_\perp}{nT}\right)_{thresh} = \left(\frac{5}{4}\frac{\Gamma_\perp}{n}\right) \left[\sqrt{1 + \frac{\left(\chi^0 \left(\alpha - \chi^0 k_r^2\right)/\nu\right)}{\left(\frac{5}{4}\frac{\Gamma_\perp}{n}\right)^2}} + 1 \right] \tag{25}$$

From here, the researchers converted Eq.(25) into a power threshold equation for convenience,

$$P_{thresh} = \frac{5}{4} \Gamma_\perp T \, A_{sep} \left[\sqrt{1 + \frac{\left(\chi^0 \left(\alpha - \chi^0 k_r^2\right)/\nu\right)}{\left(\frac{5}{4}\frac{\Gamma_\perp}{n}\right)^2}} + 1 \right] \tag{26}$$

where A_{sep} is the area of the plasma surface area at the separatrix [24]. From the analysis, Eq.(26) varied only with parameters concentrated within the edge region. This implied they were only concerned with instabilities with radial wavelengths (k_r^{-1}) between 1–10 cm. Assuming the thermal diffusivity had a range of $0.1 \le \chi^0 \le 1$ m^2/s and the α terms were comparatively large [27], the $\chi^0 k_r^2$ term had little affect on P_{thresh}. In fact, the researchers found that P_{thresh} was largely insensitive to χ^0 or k_r [27]. The parameters in Eq.(26) that tended to vary the most were the α terms and $\Gamma_\perp$ [27].

It is important to note that $P_{thresh} = P_{thresh,i} + P_{thresh,e}$ [24]. This will be very important in later use of the model; however, for we will suppress the species scripts and only concern ourselves with the total P_{thresh}. To test the P_{thresh} given by Eq.(26), the researchers tested a number of DIII-D shots [27]. The evaluated P_{thresh} was compared with the observed $P_{sep}^{\exp}$ for several shots at a time in which the plasma was about to transition from L-mode to H-mode (i.e. just prior to when ω went to zero.) The results from their first analysis looked promising [27].

Table 1: Some DIII-D shots just prior to the L-H transition (R = 1.71m – 1.79 m, a = .6 m, κ = 1.73 – 1.89) [27]

Shot #	Time (ms)	I (MA)	B (T)	P_{NBI} (MW)	n_{eped} (e19/m^3)	T_{eped} (eV)	δ	P_{sep}^{exp} (MW)	P_{thresh} (MW)
102456	1725	1.4	2.0	2.6	3.22	95	.73	1.55-1.86	1.54
97979	1900	1.4	2.0	2.0	2.59	125	.79	1.72-2.04	2.18
92079	2275	1.0	2.1	2.1	1.28	220	.37	3.99-4.06	4.00
84027	2575	1.3	2.1	2.1	2.94	144	.32	1.28-1.36	1.13

From table 1, we see that in each of the shots, as the plasma neared the L-H transition $P_{sep}^{\exp}$ approached or exceeded the calculated values of P_{thresh} [27]. The question was then posed that if this model could predict the onset of stability, it should be able to do the reverse [28]. The same analysis was carried out on several more shots, but for times just prior to when the plasma started to lose good confinement (i.e. undergo the H to L transition). Results for the analysis are listed in the table below.

Table 2: Comparing of measured non-radiative power crossing the separatrix with the predicted threshold power for times near the H – L transition. 97979[a] was a control case that had no MARFE or H-L transition [28].

Shot #	Time ms)	I (MA)	B (T)	P_{NBI} MW)	n_{eped} (e19/m^3)	T_{eped} (eV)	P_{rad}	P_{sep}^{exp} (MW)	P_{thresh} (MW)
102565	4950	1.4	2.0	4.66	6.75	170	0.69-1.33	4.21-4.85	4.60
102456	3500	1.4	2.0	2.38	2.59	150	0.79-1.13	2.48-2.82	2.36
102461	3300	1.4	1.5	2.35	7.80	170	1.29-1.35	2.11-2.17	2.18
97979[a]	3250	1.4	2.1	6.54	6.35	525	1.87-2.19	4.64-4.96	2.59

The results in table 2 show that as the plasma approached the H-L transition, P_{thresh} increased and approached $P_{sep}^{\exp}$. Thus, at both the L-H and the H-L transitions we see that $P_{sep}^{\exp} \approx P_{thresh}$ near a transition [28]. This agreement was suggestive that edge thermal instabilities play an important role for both the L-H and the H-L transitions. Moreover, the value of P_{thresh} depends on local edge parameters that vary over the course of the discharge. This suggests that this model for P_{thresh} could be used to investigate why H-L transitions occur after MARFEs.

CHAPTER 4 DIII-D EXPERIMENTAL DATA

4.1 Machine Properties

To investigate the relation between MARFEs and H-L transitions data was gathered from the DIII-D facility. D-IIID is currently the largest Tokamak in the United States and one of the largest in the world. Many features in DIII-D are being directly incorporated into the International Thermonuclear Experimental Reactor (ITER), which is expected to be the first terrestrial power producing fusion device with a Q of 10 (it will produce 10 times the amount of input energy). The Tokamak is quite large as shown in the figure below.

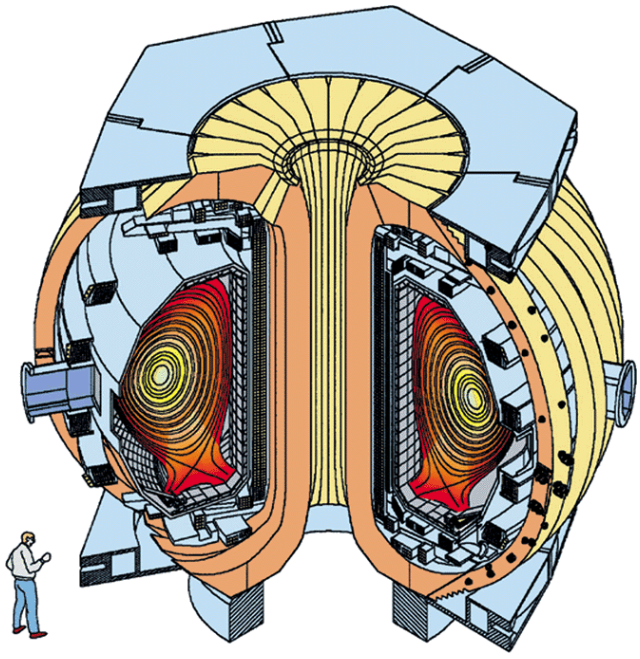

Figure 1: Cutaway of the DIII-D Tokamak in San Diego. [29]

The next figure gives us an idea of where the plasma from figure 1 resides in the Tokamak of figure 2, as well as some basic machine parameters of DIII-D.

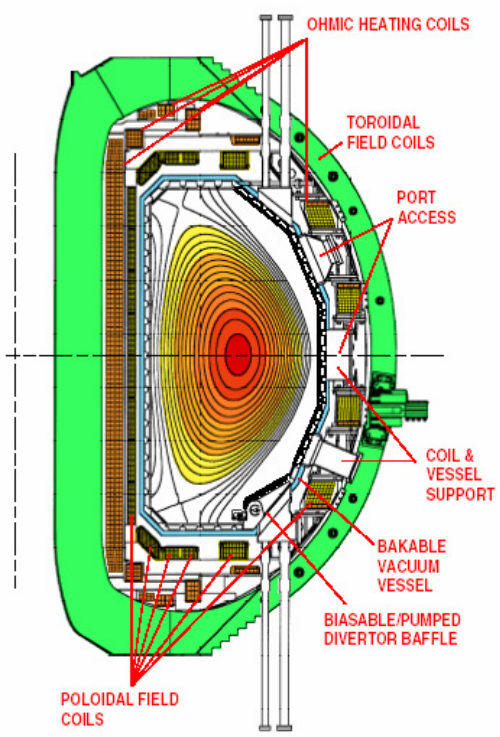

	PRESENT	PROPOSED
Major radius	1.67 m	
Minor radius	0.67 m	
Maximum toroidal field	2.2 T	
Available OH flux	10.5 V-s	
Maximum plasma current*	3.0 MA	3.5 MA
Neutral beam power (80 keV)	20 MW	
RF power (110 GHz)	0.5 MW	4 →10 MW
RF power (30–120 MHz)	2 → 6 MW	8 MW
Current flattop (divertor at 2 MA)	5 s	10 s

*Divertor operation; Limiter operation of 3 MA achieved.

Figure 2: Cross Section with basic machine parameters [30].

4.2 Diagnostics

The shots used in our analysis (discussed in a later chapter) were chosen because they each experienced detachment, divertor MARFE, core MARFE, and H-L transition. All three of these discharges were continually gas fueled in an attempt to achieve a high density. As seen in table 4, shot 92972 and 92976 were nearly identical except for

the toroidal magnetic field which subsequently altered q95. Shot 96887 was similar to the two previously mentioned shot, except it had a higher neutral beam power and gas fueling rate. Additionally, each of the shots were chosen because the plasma was in position to take advantage of certain diagnostic tools.

Table 3: Parameters of gas fueled D-IIID shots that underwent an H-L transition immediately following core MARFE formation.

Shot #	*Time (ms)*	*I (MA)*	*B(T)*	q95	P_{NBI} *(MW)*	n_{eped} *(e19/m^3)*	T_{eped} *(eV)*	*nebar (e19/m^3)*
92976	2500 to 3212	1	2.1	6.2	5.2	4.1 to 4.4	218 to 187	5.0 to 6.1
92972	2500 to 3325	1	1.1	3.2	5.0	5.5 to 6.2	414 to 168	6.3 to 8.4
96887	2500 to 3650	1.7	2.1	3.2	8.5	9.6 to 11.3	440 to 231	10.1 to 12.7

4.2.1 Langmuir Probes

The first diagnostic tool we will discuss are the Langmuir probes in the DIII-D divertor target plates. These are used to precisely measure local density, temperature, particle flux, edge current, and floating potential just in front of the target plate [31]. Probe data was analyzed to determine an estimate of when the plasma partially detached

inevitably forming a divertor MARFE. For 92976 it was determined that the divertor MARFE occurred at around 2800 ms. In 92972, probe data indicated the divertor MARFE occurred at around 2790 ms. For shot 96887, the divertor MARFE occurred around 2390 ms. While the Langmuir probes are useful for determining when the plasma detaches from the divertor plate prior to Divertor MARFE and Divertor MARFE formation, they can not provide any information about the MARFE formation which takes place at the X-Point.

4.2.2 Thomson Scattering

For determining core MARFE formation, we will first discuss the use of Thomson Scattering in DIII-D. One can learn a great deal from the scattering of electromagnetic radiation on a plasma. For DIII-D, the Thomson Scattering system is an array of 20 Hz Nd:YAG lasers directed in a vertical pattern from a port outside the chamber towards the plasma. The lasers interact with the electrons. The change in wavelength allows one to determine what the temperature of the plasma is. A distribution function of electron density can also be determined from the light that does not scatter [32].

For our analysis, we chose discharges in which there was a Thomson Scattering channel near the X-point. The

yellow and red dots in the figure below indicate the Thomson Scattering chords. The red dot is the channel m122. The yellow dot immediately above the red dot is channel m119. For shots 92976 and 92972, the red dot lies just outside the separatrix, therefore the channel m119 is used. In shot 96887, the red dot is just above the X-point and inside the separatrix, so the channel m122 was used.

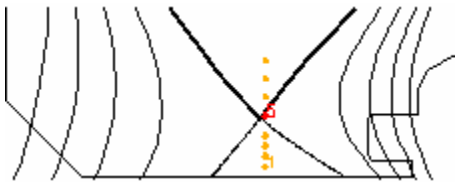

Figure 3: Thomson Scattering Chords for shot 92972 at 3325 ms.

Use of this channel displays the collapse of the electron temperature and a spike in the electron density inside the separatrix [19]. For example, in figure 4 there is a spike in density and a collapse in the electron temperature between the 3050 and 3100 time-slices, which is indicative of MARFE formation.

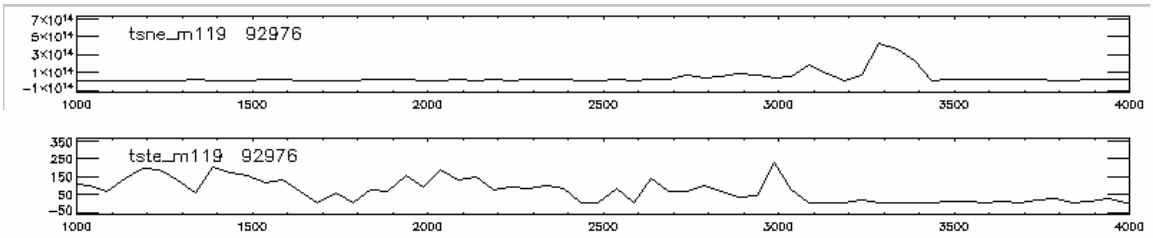

Figure 4: Thomson scattering data for electron temperature and density passing through channel m119 (just inside separatrix just outboard of the X-point) in shot 92976.

Similarly, figure 5 shows a cool dense region forming near the X-point between times 3100 and 3325 ms in shot 92972.

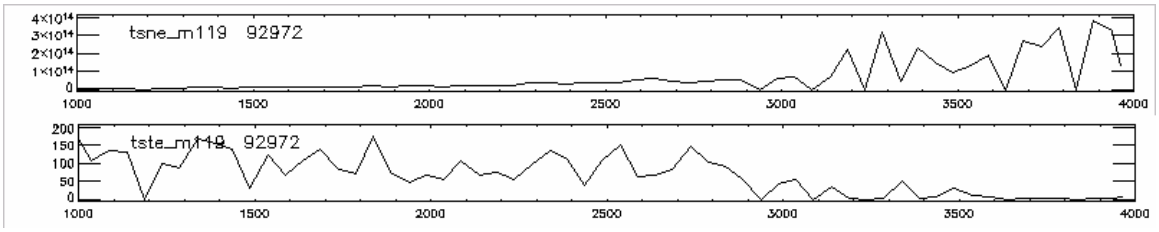

Figure 5: Thomson scattering data for electron temperature and density passing through channel m119 (just inside separatrix just outboard of the X-point) in shot 92972.

While not as clear as 92976 and 92972, figure 5 exhibits a collapse in the electron temperature and a spike in the electron density somewhere between 3200 and 3650 ms in shot 96887.

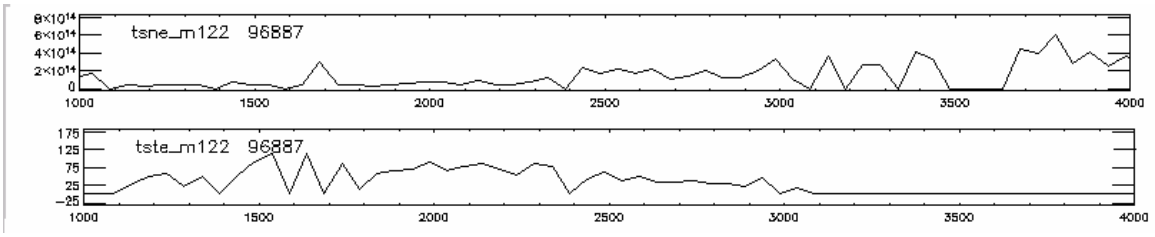

Figure 6: Thomson scattering data for electron temperature and density passing through channel m122 (just inside separatrix just outboard of the X-point) in shot 96877.

4.2.3 Bolometer Array

Another important diagnostic tool is the bolometer array. The bolometer array is simply an array of heat sensors set around the chamber [31].

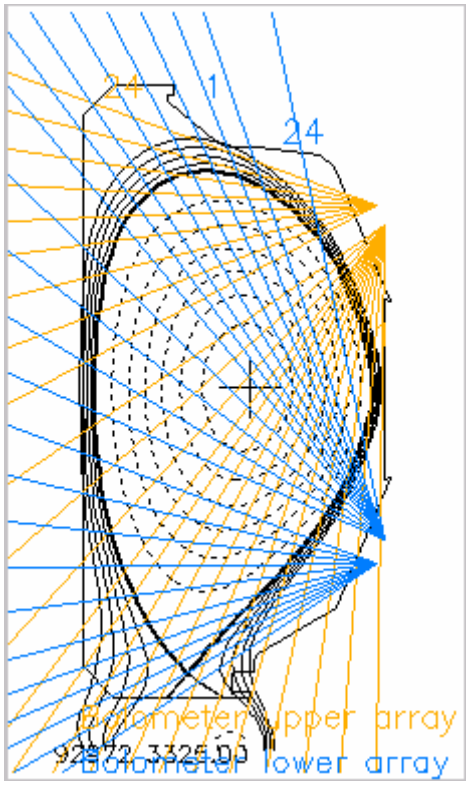

Figure 7: DIII-D Bolometer Array

A voltage change is picked up across the bolometer. This is then interpreted as a change in the heat measured on the bolometer, which is further interpreted as a change in radiation from within the plasma along the line of sight of the chord [33]. The bolometer array can be used the find the radiated power distribution from a certain channel, or the total power loss due to radiation.

Each figure below comes from data gathered from the fourth chord in the lower bolometer array. Looking at figure 7, this is the fourth blue line from the bottom. Each of the figures below show a power spike near the times

that the Thomson Scattering data revealed a core MARFE took place. In 92976, the power spike is most pronounced just after 3200 ms.

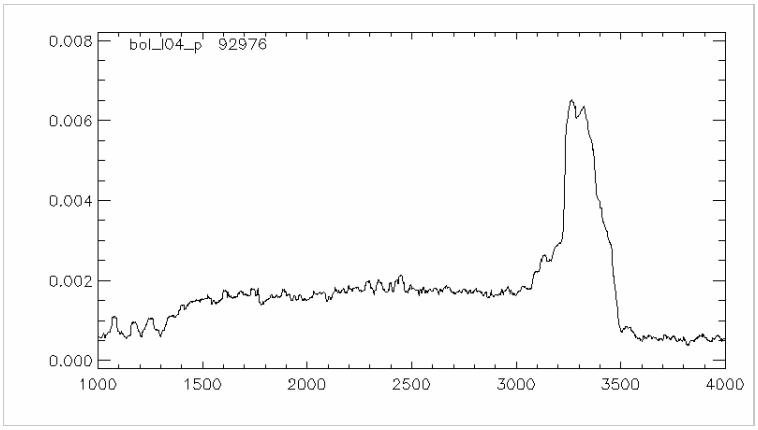

Figure 8: Bolometer reading from lower array channel 4 in shot 92976.

Figure 9 shows the bolometer reading for shot 92972. The first large spike in radiative power occurred around 3300 ms. Due to scaling, this is not as pronounced as figure 8, but the spike is significant.

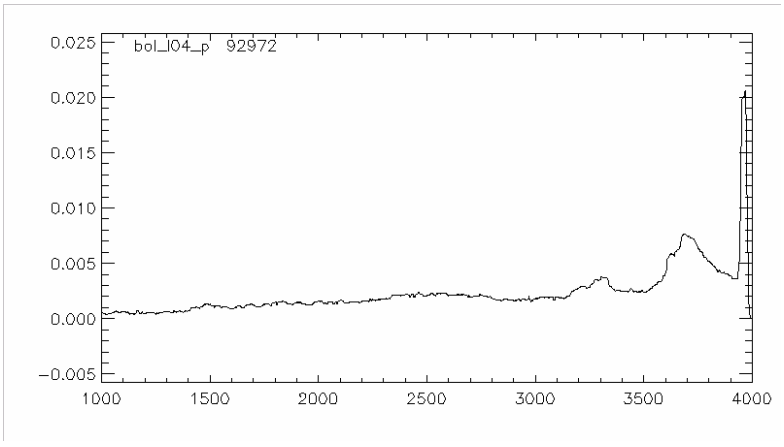

Figure 9: Bolometer reading from lower array channel 4 in shot 92972.

Figure 10 shows a very large spike in radiated power near 3600 ms. This coincides with the Thomson Scattering data indicates a core MARFE took place between 3200 and 3650 ms.

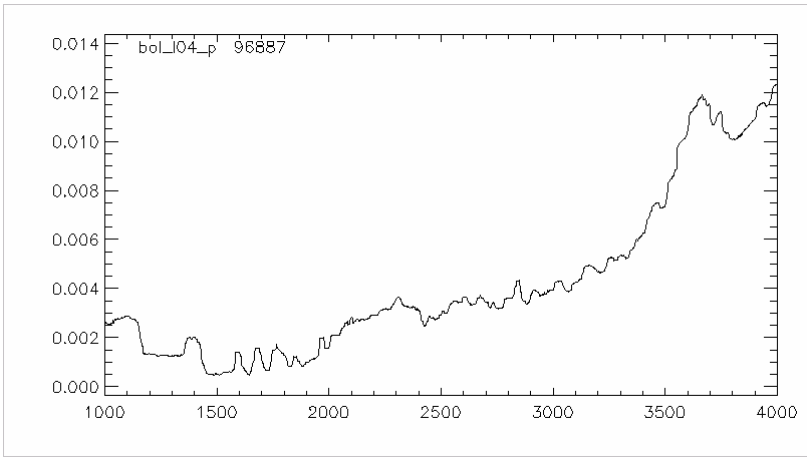

Figure 10: Bolometer reading from lower array channel 4 in shot 96887.

The information from the entire bolometer array can also be Abel-inverted to give us a two dimensional picture of the areas radiating the most power. This is particularly useful when looking at the evolution of a discharge.

Here is an example using shot 92972. Comparing figure 11 with figures 5 and 9, we can visualize core MARFE formation. At 3100 ms, the core MARFE is beginning to form. The electron temperature is low, but the density has not increased yet. Just after 3100 ms, there is a spike in the electron density, yet the temperature remains fairly constant for another 100 ms or so. The bolometer readings however show a constant increase in radiated power for

another 200 ms. Data from Thomson scattering and bolometers can only give us estimates for when MARFEs form. To ascertain the moment a core MARFE crosses the X-point and causes an H-L transition, data pertinent to plasma confinement is needed.

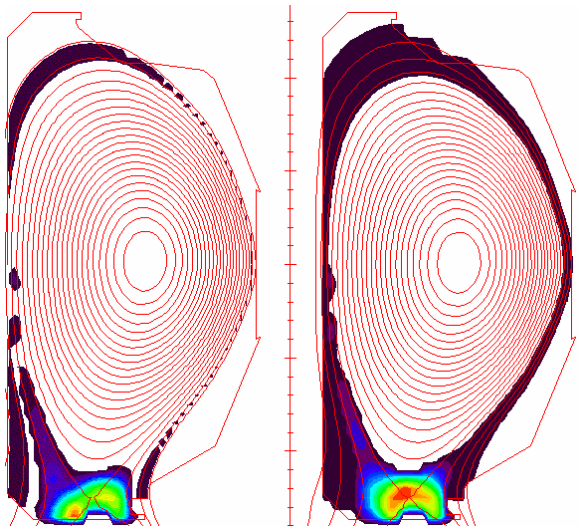

Figure 11: 2D power radiation profile at time 3100 for the first and at time 3325 for the second

4.2.4 Filterscopes

The H-L back transition is identified experimentally primarily by the deuterium atomic emission line (6562 Å) or (D_α light) observed from an array of filterscopes [34] (see figure 12). The intensity of the D_α light varies directly with the deuterium neutral density, which in turn varies directly with the plasma ion flux to the wall. A sharp increase in the D_α light indicates a sharp increase in neutral deuterium, indicating a sharp increase in the

escaping deuterium ion flux to the wall associated with a sharp drop in plasma confinement. Therefore, just after an H-L transition, there is a significant spike in the D_α light.

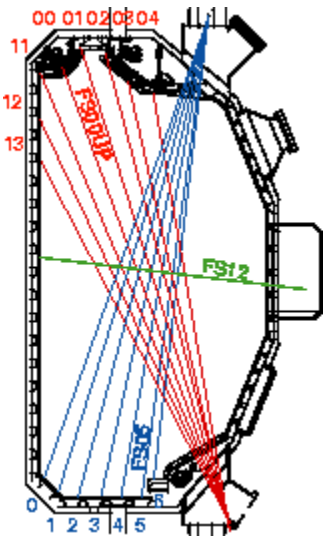

Figure 12: View of filterscopes in the poloidal plane in the DIII-D [34].

The figures below display filterscope data (D_α light emissions) as seen from the number 3 blue channel in figure 12. For shot 92976, the D_α light increases significantly just after 3200 ms indicating an H-L transition has taken place.

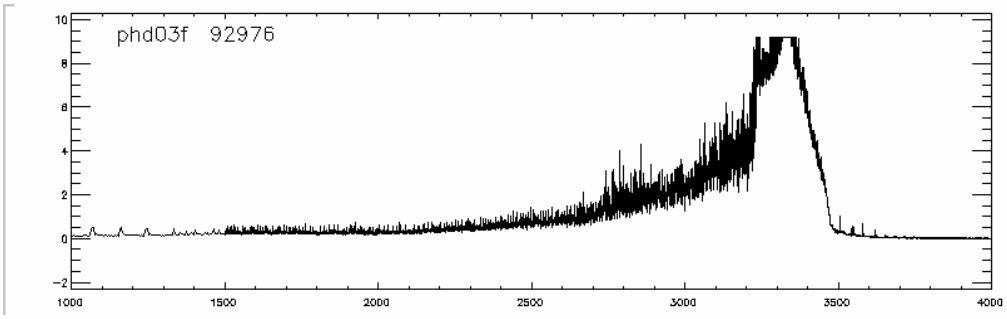

Figure 13: Filterscope data from a channel passing near the X-point in shot 92976.

The greatest change in D_α light in 92972 happens near 3320 ms, suggesting an H-L transition took place in the vicinity. We chose this to be 3323 ms.

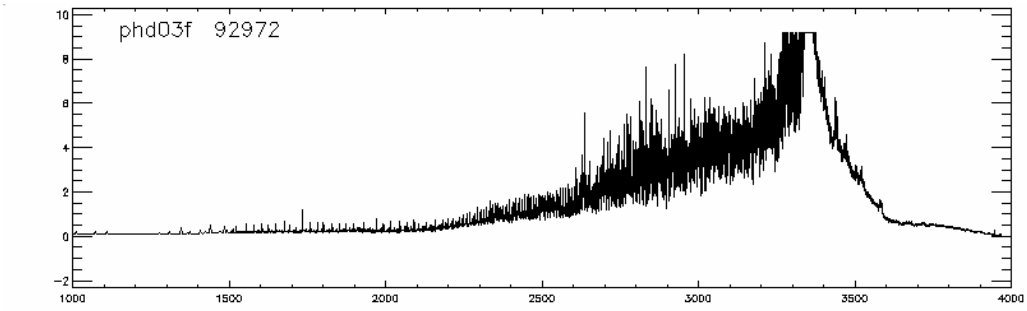

Figure 14: Filterscope data from a channel passing near the X-point in shot 92972.

Of the three shots chosen, the H-L transition is hardest to see in 96887 from the filterscope channel selected. The filterscope chord chosen shows a relatively constant loss in confinement; however, near 3650 ms there is a noticeable spike in D_α light emission.

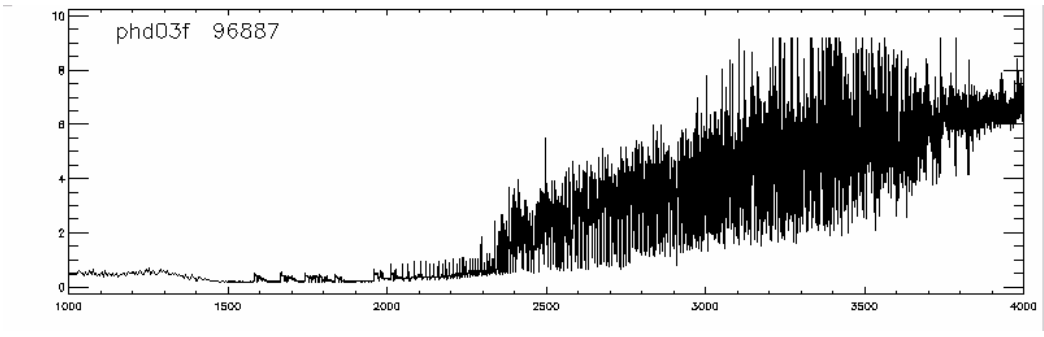

Figure 15: Filterscope data from a channel passing near the X-point in shot 96887.

CHAPTER 5 MODELING EXPERIMENT

To evaluate the parameters in Eq.(26), measured values of density and temperature can be use, but it is necessary to calculate the fueling of the edge pedestal and the core plasma by injected and recycling neutrals in order to evaluate the outward particle flux ($\Gamma_{\perp}$) from the particle balance on the core. The neutral influx was also necessary in order to evaluate the ionization, charge exchange, and elastic scattering frequencies that appear in the α-terms of Eq.(17) and Eq.(18). In order to calculate the transport of neutral atoms recycling from the divertor plate through the lower divertor region and back across the separatrix into the plasma edge, it was necessary also to calculate the plasma density and temperature in the divertor region, since these quantities are not readily measured except at the specific divertor TS locations and at the probe locations just in front of the wall. Thus, a plasma model and a neutral fueling and recycling calculation were required in order to evaluate the outward particle flux in Eq.(26) [35].

To model the plasma, an initial plasma core power and particle balance was performed. The power balance was found by equating the net heating (Ohmic plus external heating

less core impurity and bremsstrahlung radiation) to the power flux from the core into the scrape off layer (SOL)[35]. This power out-flux ($Q_\perp$) was then related to the average temperature, density, and energy confinement time, τ_E

$$T_{av} = \frac{Q_\perp \tau_E A_p}{3 n_{av} V_p} \tag{27}$$

where A_p and V_p are plasma surface area and volume, respectively. τ_E was found using the ITER89P scaling law[36] with an H_{89} enhancement factor; which means $\tau_E = H_{89}\tau_{89}$, where

$$\tau_{89} = .048 I_{MA}^{0.85} R_m^{1.2} B_T^{0.2} a_{20}^{0.1} \left(\frac{A_{amu}\kappa}{P_{MW}} \right)^{0.5} \tag{28}$$

where κ is the plasma elongation, and the subscripts indicate the units of global parameters[36].

The average core plasma density (n_{av}) was found by equating the total core fueling by neutral influx from the SOL plus other fueling sources to the ion out-flux ($\Gamma_\perp$) into the SOL. This was then related to the ion out-flux to the average ion density and the particle confinement time

$$n_{av} = \frac{\Gamma_\perp \tau_n A_p}{V_p}. \tag{29}$$

The particle confinement time is taken from the scaling developed from measurement of density die-away after pellet injection in the DIII-D tokamak [37]

$$\tau_n = H_n \tau_n^0 = H_n \times 0.51I. \tag{30}$$

Having modeled the region from the core to the SOL, a model describing the region from the SOL to the divertor was needed. For this, a two-point, two dimensional SOL-DIV model was used. The "two-point" refers to the integration over the divertor of the particle, momentum, and energy balances on the plasma outside the separatrix in the divertor region, leading to equations that can be solved for the densities and temperatures at two points, just in front of the divertor target and upstream near the separatrix . The "two-dimensional" refers to the transport calculation within the divertor region of neutral deuterium that has either recycled from the divertor target or been injected into the plenum region outside the plasma. This model has been benchmarked by comparison with a 2D plasma fluid/Monte Carlo neutrals calculation of DIII-D plasmas [38].

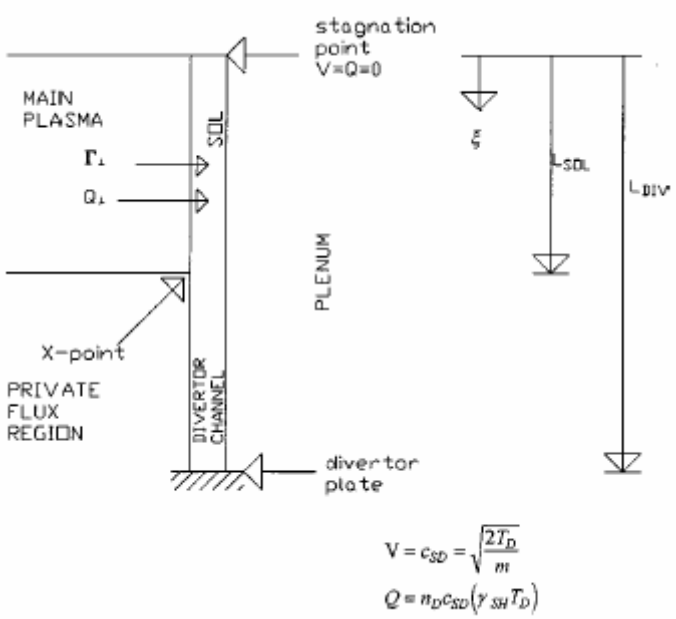

Figure 16: Slab model for SOL/DIVERTOR plasma Calculation.

Figure 15 depicts the slab model for the SOL/DIV model used in our analysis. Neutrals modeled from the SOL/DIV model were fed back into the particle balance mentioned before. To account for neutral gas sources diffusing out of the material walls, the injected gas sources were adjusted until the calculated density in the plasma matched the experimental density; i.e. the fueling was correctly calculated.

CHAPTER 6 Model Confirmation

The general modeling procedure described in Chapter 5 has been used extensively to supplement experimental data by modeling the background divertor plasma and neutral transport in the divertor in the analysis of the onset of the Divertor MARFE and MARFE thermal instabilities in DIII-D [39]. To further increase confidence in our modeling techniques for the analysis P_{thresh}, we will analyze these two additional thermal instabilities simultaneously for the same shots. First, however, we must discuss the thermal instability onset predictions for MARFEs [39] and divertor MARFEs [39].

6.1 Divertor MARFE Onset

The divertor MARFE onset was modeled by performing a one dimensional (density, momentum, and energy equations) linear analysis of stability of the divertor and SOL plasma to long parallel wavelength instabilities [40]. This leads to a complex dispersion relation which must be solved numerically to determine the growth rate, ω_{DIV}, for long wavelength thermal instabilities in the divertor corresponding to the divertor MARFE. When ω_{DIV} is negative,

the plasma is stable and no divertor MARFE is predicted. When ω_{DIV} goes positive, this indicates the onset of a divertor MARFE.

6.2 Core MARFE Onset

The core MARFE is modeled in a similar fashion [40]. Researchers at Georgia Tech have previously shown theoretically and demonstrated numerically that the $k_{\|} = (m - nqB_{\theta}/B)/qR \approx 0$ two-dimensional edge localized modes are the first to become unstable in MARFE formation because of parallel heat conduction for finite $k_{\|}$ modes [40,41,42]. By performing a linear analysis of the stability of a poloidally uniform plasma edge density and temperature distribution to $k_1 \approx 0$ edge-localized modes, a dispersion relation for the onset of parallel instabilities along field lines in the region just inside the separatrix was found [40]. This dispersion relation can be used to predict the density at which a core MARFE should take place (n_{MARFE}). A ratio of the experimental value for the average electron density (n_e) to n_{MARFE} can be defined (MI). When MI is greater than or equal to one, a core MARFE is predicted. Both the divertor and core MARFE models have been used successfully

to predict the onset of instabilities in experiments at DIII-D [43]

6.3 Values MI and ω_{DIV}

Three times where chosen from each shot to exhibit the evolution of the P_{thresh} from Divertor MARFE onset to H-L transition in anticipation of determining a causative relation between the core MARFE and the H-L transition. The analysis of P_{thresh} (discussed in the next chapter) was carried out for each at each of these times simultaneously with the models used to find MI and ω_{DIV}. The table below illustrates how these models have instilled confidence in our model for P_{thresh}.

Since the calculation for P_{thresh} involves a linear analysis of thermal instabilities in the edge, many of the same plasma parameters used in its calculation are identical to the prediction for the onset of the Divertor MARFE and MARFE thermal instabilities. Therefore, if MI and ω_{DIV} are modeled correctly then the plasma should be modeled correctly for the P_{thresh} calculation. Table 4 shows that in each of the time-slices, MI and ω_{DIV} coincide with the experimental data. ω_{DIV} is negative when no divertor MARFE has occurred and positive when one has occurred, and MI is less than one before the core MARFE has been predicted.

Table 4: Divertor and core MARFE prediction and observation in three DIII-D shots that underwent H-L transitions following core MARFE formation.

TIME ↓↓↓

92976 *TIME(ms)*	$\omega_{DIV}(10^5/s)$	$MI=n_{exp}/n_{marfe}$
2500	-93	.23
2962-3000	DIVERTOR MARFE	
3000	25	.65
3050-3100	CORE MARFE	
3212	46	1.8
3230	H-to-L TRANSITION	

TIME ↓↓↓

92972 *TIME(ms)*	$\omega_{DIV}(10^5/s)$	$MI=n_{exp}/n_{marfe}$
2500	-36	.39
2750-2790	DIVERTOR MARFE	
3000	-4.8	.80
3100-3325	CORE MARFE	
3325	27	1.5
3323	H-to-L TRANSITION	

TIME ↓↓↓

96887 *TIME(ms)*	$\omega_{DIV}(10^5/s)$	$MI=n_{exp}/n_{marfe}$
2390	DIVERTOR MARFE	
2500	14	.43
3200	22	.53
3200-3650	CORE MARFE	
3650	65	2.2
3653	H-to-L TRANSITION	

In shot 92976, the divertor MARFE was observed between 2962–3000 ms. A calculation of $\omega_{DIV} < 0$ at 2500 ms indicates that a divertor MARFE has not taken place at that time, and a prediction of MI < 1 indicates that the core MARFE has not yet formed. At 3000 ms, ω_{DIV} has become positive, predicting that the divertor MARFE has formed, in agreement with experimental observations. However, the MI < 1 predicting the core MARFE has not yet formed at 3000 ms is in agreement with experiment. At 3212 ms, the larger ω_{DIV} gives a stronger prediction of divertor MARFE formation, and MI > 1 predicts that the core MARFE has formed. This is consistent with the experimental observation of core MARFE formation at 3050–3100 ms.

In shot 92972, the divertor MARFE was observed between 2750–2790 ms. A calculation of $\omega_{DIV} < 0$ at 2500 ms indicates that a divertor MARFE has not taken place at that time, and a prediction of MI < 1 indicates that the core MARFE has not yet formed. At 3000 ms, ω_{DIV} has nearly becomes positive, predicting that the divertor MARFE has formed, in agreement with experimental observations. However, the MI < 1 predicting the core MARFE has not yet formed at 3000 ms is in agreement with experiment. At 3325 ms, the larger ω_{DIV} gives a stronger prediction of divertor MARFE formation, and MI > 1 predicts that the core MARFE has formed. This is

consistent with the experimental observation of core MARFE formation at 3100–3325 ms.

In shot 96887, the divertor MARFE was observed around 2390 ms. A calculation of $\omega_{DIV} > 0$ at 2500 ms indicates that a divertor MARFE has taken place at that time, and a prediction of MI < 1 indicates that the core MARFE has not yet formed. At 3200 ms, the larger ω_{DIV} gives a stronger prediction of divertor MARFE formation, in agreement with experimental observations. However, the MI < 1 predicting the core MARFE has not yet formed at 3200 ms is in agreement with experiment. At 3650 ms, the larger ω_{DIV} gives a stronger prediction of divertor MARFE formation, and MI > 1 predicts that the core MARFE has formed. This is consistent with the experimental observation of core MARFE formation at 3200–3650 ms.

CHAPTER 7 ANALYSIS OF P_{THRESH}

As mentioned early, three time slices were chosen from each of the shots to show the evolution P_{thresh}. The first time-slice chosen is at a time prior to plasma detachment and Divertor MARFE formation. The second time slice is at a time after the Divertor MARFE but before the core MARFE. The third and final time slice was chosen to be at a time just prior to the H-L transition when the core MARFE is well established and about to cross the separatrix. Table 5 shows the results of the P_{thresh} analysis using the modeling techniques discussed in chapter 5. P_{thresh} is being compared to the non-radiative power crossing the separatrix, which is found by performing a power balance on the plasma

$$P_{sep}^{\exp} = P_{OH} + P_{NBI} - \frac{dW}{dt} - P_{rad} \tag{31}$$

where P_{rad} is the power radiating from within the core and $\frac{dW}{dt}$ is the change in stored thermal energy.

Table 5: P_{thresh}^{theory} and P_{sep}^{exp} evolution during three DIII-D shots that underwent H-L transitions following core MARFE. (All Units are in MW)

TIME ↓	**92976** *TIME(ms)*	P_{rad}	P_{NBI}	$\frac{dW}{dt}$	P_{OH}	P_{sep}^{exp}	P_{thresh}
	2500	.54	5	0	.30	**4.8**	**2.5**
	2962-3000	DIVERTOR MARFE					
	3000	.39	5	0	.58	**5.2**	**3.0**
	3050-3100	CORE MARFE					
	3212	1.4	5	0	.63	**4.2**	**4.1**
	3230	H-to-L TRANSITION					
TIME ↓	**92972** *TIME(ms)*	P_{rad}	P_{nbi}	$\frac{dW}{dt}$	P_{OH}	P_{sep}^{exp}	P_{thresh}
	2500	.62	5.2	0	.35	**4.9**	**3.5**
	2750-2790	DIVERTOR MARFE					
	3000	.87	5.2	0	.45	**4.8**	**3.7**
	3190	CORE MARFE					
	3325	1.29	5.2	0	.55	**4.5**	**4.6**
	3323	H-to-L TRANSITION					
TIME ↓	**96887** *TIME(ms)*	P_{rad}	P_{nbi}	$\frac{dW}{dt}$	P_{OH}	P_{sep}^{exp}	P_{thresh}
	2390	DIVERTOR MARFE					
	2500	.8	8.5	0	.21	**7.9**	**6.1**
	3200	1.09	8.5	-.46	.37	**8.2**	**6.8**
	3240	CORE MARFE					
	3650	1.2	8.5	-.23	.95	**8.5**	**8.8**
	3653	H-to-L TRANSITION					

From table 5, we see that P_{rad} typically appears to increase at a constant rate. This normally causes a constant reduction in P_{sep}^{exp}; however, as table 5 also shows this is not always the case. In certain situations the Ohmic heating power heating power input can increase more rapidly than the radiation power loss.

A more important observation is what is happening to P_{thresh} as the shot evolves. We see that from the first to the second time slice, P_{thresh} increases only slightly while

remaining less than $P_{sep}^{\exp}$. In Eq.(1), the density is the only changing factor, and since this is a continuously gas fueled shot, the density is slowly increasing. However, from the second to the third time slice, over which interval the MARFE occurs, P_{thresh} is no longer increasing slightly. There is a relatively large spike in P_{thresh} compared with the change in P_{thresh} from the first to the second time. To see why this is, we broke P_{thresh} down into its components.

Table 6: Evolution of edge pedestal parameters during three DIII-D shots that underwent H-L transitions following a core MARFE.

92976 *TIME(ms)*	$S_{recyc}(10^{20}/s)$	n_{ped} $(10^{20}m^{-3})$	T_{eped}(eV)	f_0 (%)	α_i $(10^3 s^{-1})$	α_e $(10^3 s^{-1})$	$\Gamma_\perp(10^{20}/s)$
2500	.64	.41	218	.84	.37	.40	1.6
2962-3000	DIVERTOR MARFE						
3000	1.4	.43	212	1.7	.88	1.3	3.0
3050-3100	CORE MARFE						
3212	3.9	.44	187	3.7	2.3	2.4	6.9
3230	H-to-L TRANSITION						
92972 *TIME(ms)*	$S_{recyc}(10^{20}/s)$	n_{ped} $(10^{20}m^{-3})$	T_{eped}(eV)	f_0 (%)	α_i $(10^3 s^{-1})$	α_e $(10^3 s^{-1})$	$\Gamma_\perp(10^{20}/s)$
2500	.40	.59	414	.48	.26	.29	1.1
2750-2790	DIVERTOR MARFE						
3000	1.1	.62	212	.91	.48	1.0	2.7
3190	CORE MARFE						
3325	7.2	.55	168	2.3	1.6	1.6	12
3323	H-to-L TRANSITION						
96887 *TIME(ms)*	$S_{recyc}(10^{20}/s)$	n_{ped} $(10^{20}m^{-3})$	T_{eped}(eV)	f_0 (%)	α_i $(10^3 s^{-1})$	α_e $(10^3 s^{-1})$	$\Gamma_\perp(10^{20}/s)$
2390	DIVERTOR MARFE						
2500	2.1	.99	440	.46	.45	.46	5.3
3200	2.5	.96	450	.56	.54	.55	6.1
3240	CORE MARFE						
3650	6.7	1.13	231	.70	.90	1.1	13
3653	H-to-L TRANSITION						

S_{recyc} in the above table is equal to $\Gamma_o^{in} A_{sep}$, or the neutral particle influx. We clearly see from the results that just prior to the core MARFE there is an abrupt jump in the S_{recyc}, and therefore a jump in the neutral concentration in the edge (f_o). From Eq.(4), we can see that the onset of an increase in $\Gamma_o^{in} A_{sep}$ can dramatically increase the ion outflux across the separatrix. This, in turn, causes the abrupt change in P_{thresh}.

The increase in f_o also has an effect on the α terms. If we recall from earlier in Eq.(5) and Eq.(6), $\nu_{ion} \equiv n_o \langle \sigma v \rangle_{ion}$ and $\nu_{at} \equiv n_o^{cold} (\langle \sigma v \rangle_{cx} + \langle \sigma v \rangle_{elast})$. The increase in f_o is an increase in the neutral densities. It therefore becomes apparent that the increase in the neutral concentration also has the effect of increasing the α terms. In addition, the neutral concentration in the edge also affects the carbon radiation emissivity, which causes an additional increase in α_e.

CHAPTER 8 SUMMARY & CONCLUSIONS

We have investigated the experimental observation that an H-L transition follows immediately after core MARFE formation by evaluating a prediction for the threshold non-radiative power crossing the separatrix, P_{thresh}, that is required to maintain H-mode. We then compared this with the measured value of non-radiative power crossing the separatrix, P_{sep}^{exp}, as three different DIII-D discharges evolved. The evolution of the physical parameters that are involved in P_{thresh} and P_{sep}^{exp} provide an interpretation of why an H-L transition follows immediately after formations of a core MARFE.

From these results, we conclude that the main reason that an H-L transition follows the onset of a MARFE is because the increased neutral influx associated with the MARFE formation causes a sharp reduction in the threshold non-radiative power crossing the separatrix that is required for the plasma to remain in H-mode.

A secondary reason that an H-L transition follows MARFE onset is the reduction of non-radiative power crossing the

separatrix as a result of the increased radiation from inside the separatrix when the MARFE is formed.

Appendix

The following are figures showing the data gathered from DIII-D used to find the gradient scale lengths for the electron density and temperature, and ion temperature.

Electron Density

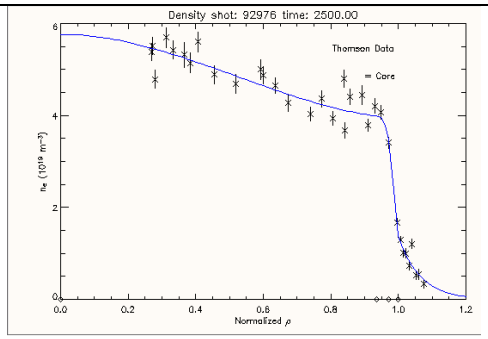

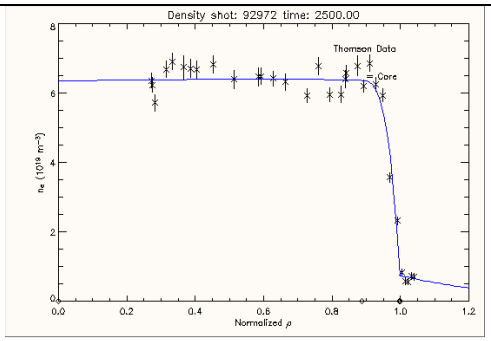

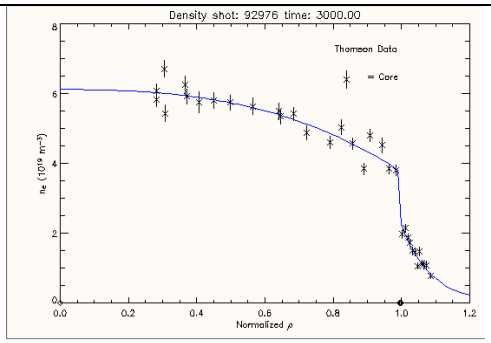

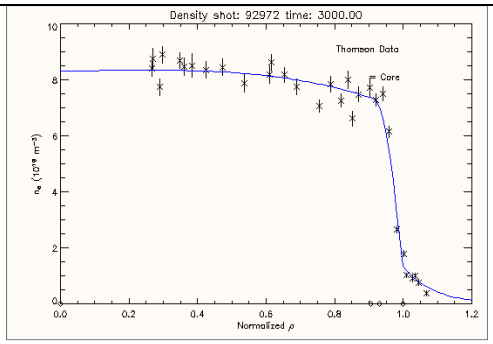

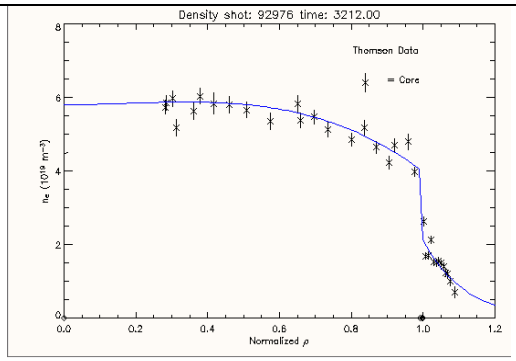

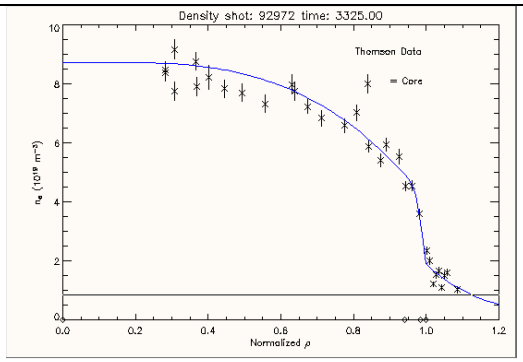

Electron Density

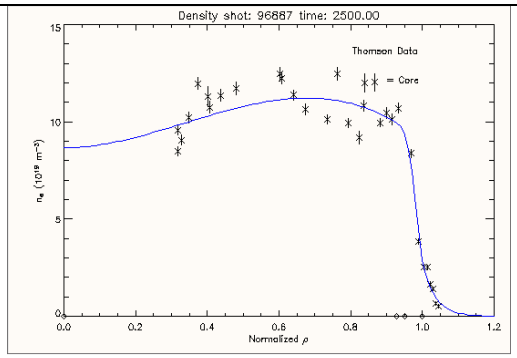

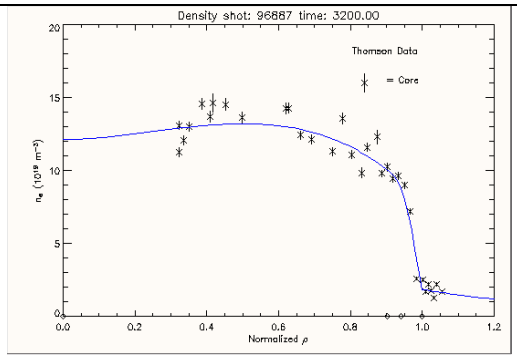

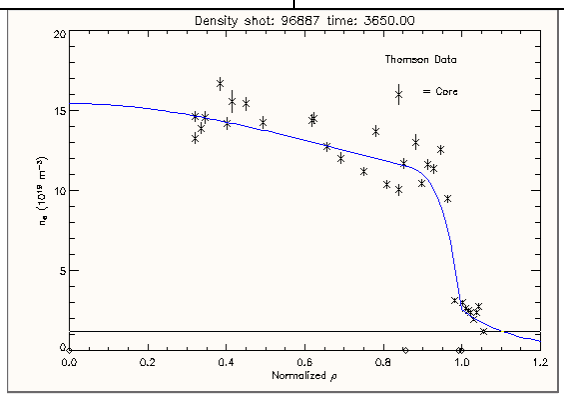

Electron Temperature

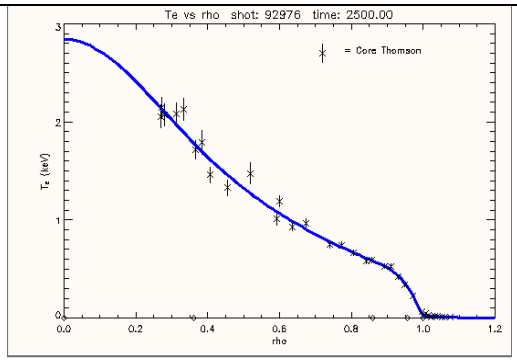

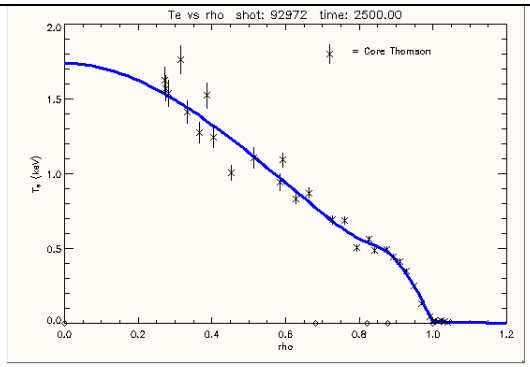

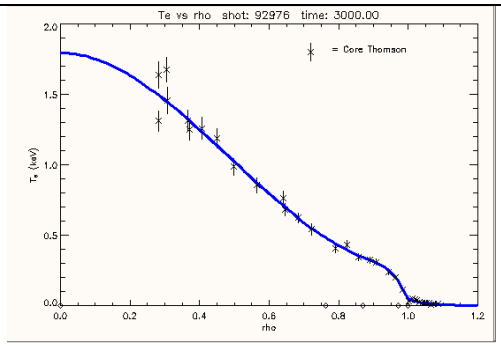

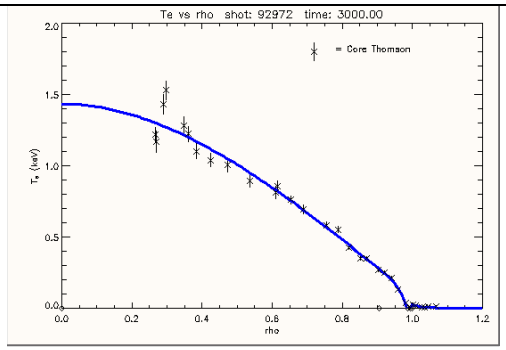

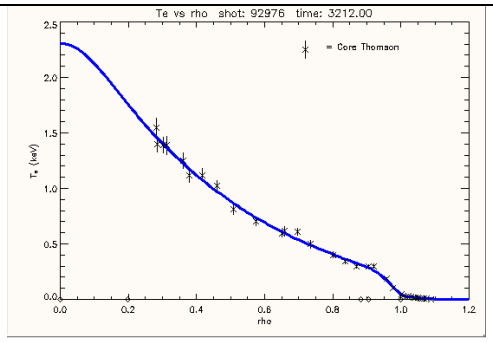

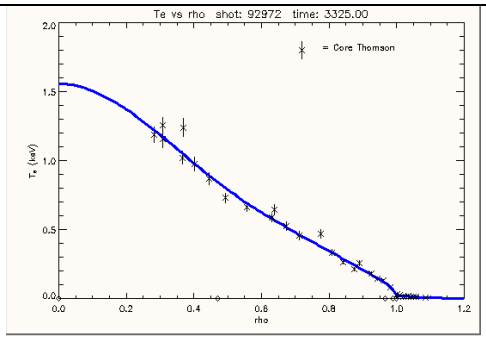

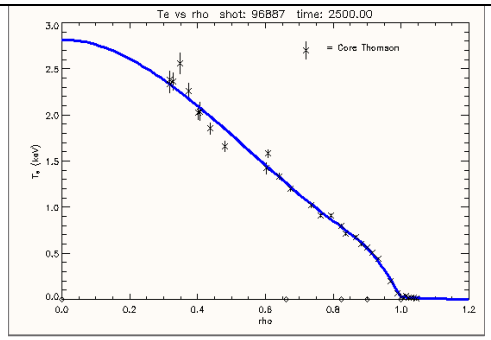

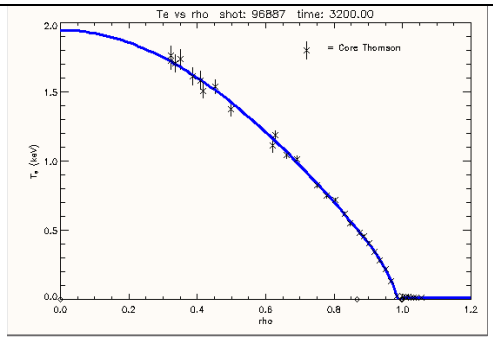

Electron Temperature

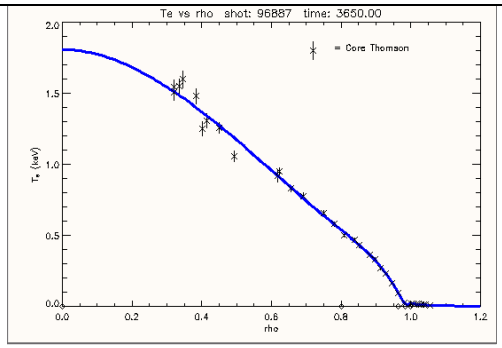

Ion Temperature

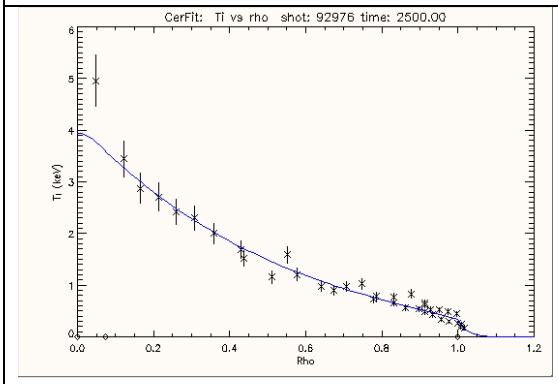

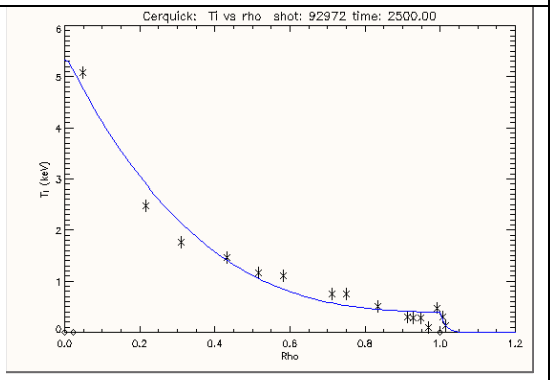

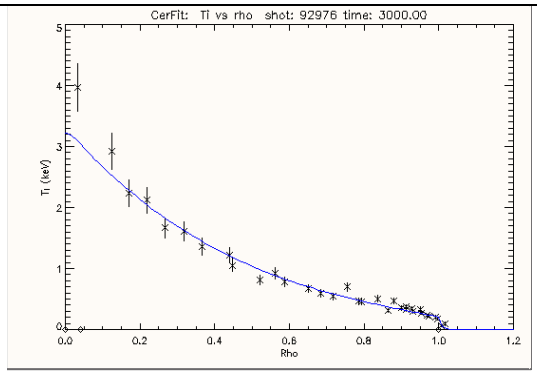

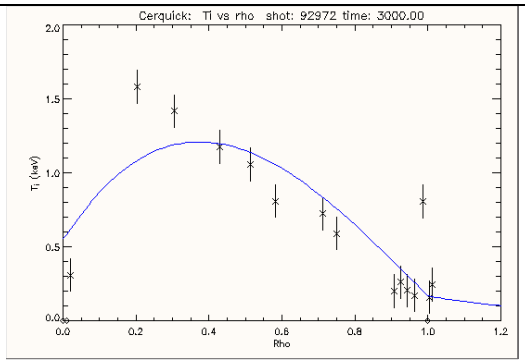

Ion Temperature

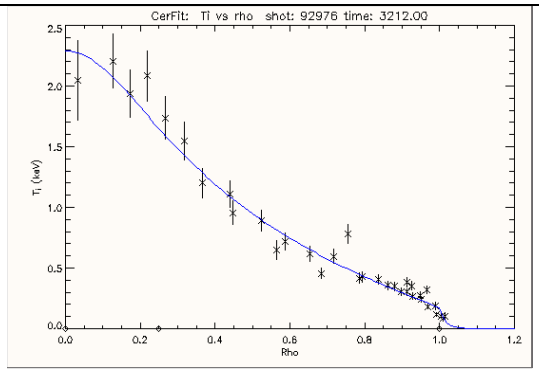

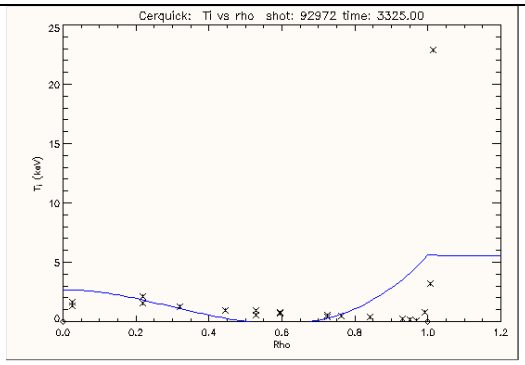

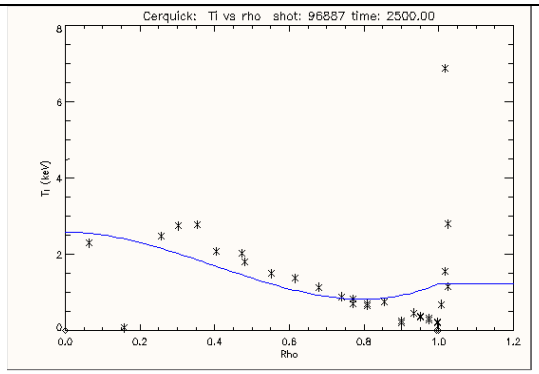

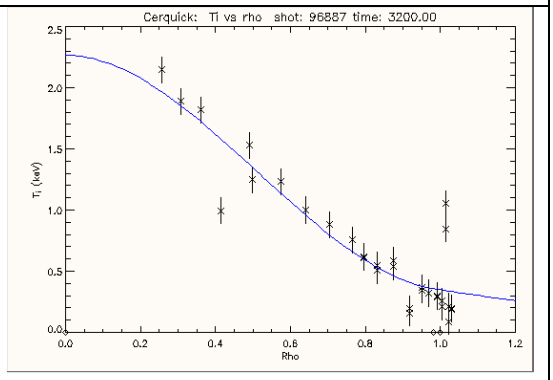

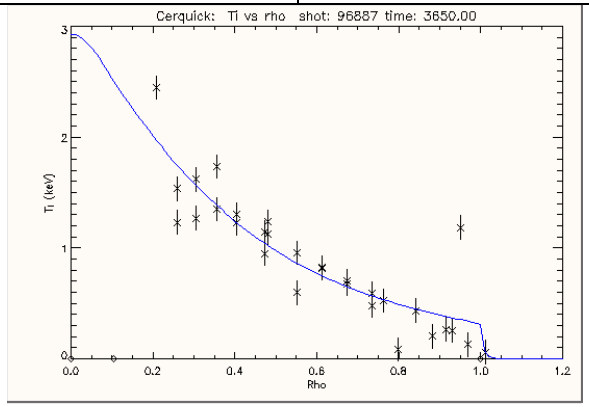

REFERENCES

1) W.M. Stacey, Phys. Plasmas, vol. 9, pp 2692-2706 (2002).

2) T.W. Petrie, A.G. Kellman, M. Ali Mahdavi, Nucl. Fusion, vol 33, no. 6, 929-952 (1993).

3) H. Thomsen, et. al., Nucl. Fusion, 44, pp 820-826 (2004).

4) F. Alladio, R. Bartirorno, B. Casali, et al., Phys. Lett., 90A, 405 (1982).

5) H. Niedermeyer, K. H. Behringer, K. Bernhardi, et al., Proc. 11th Euro. Conf. Control. Fusion Plasma Phys., Aachen, Europhysics Conf. Abstracts 7D-1, p. 43 (1983).

6) S. M. Kaye, M. Bell, K. Bol, et al., Proc. 11th Euro. Conf. Control. Fusion Plasma Phys., Aachen, Part II, p. O-10 (1983).

7) D. R. Baker, R. T. Snider and M. Nagami, Nucl.Fusion, 22, 807 (1982).

8) M. Z. Tokar, Sov. Phys. Dokl., 29, 928 (1984).

9) M. Z. Tokar, Phys. Scr. 31, 411 (1985).

10) V. Nedospasov and M. Z. Tokar, Sov. Phys. Dokl., 31, 344 (1986).

11) B. Lipschultz, J. Goetz, B. LaBombard, et al., J. Nucl. Mater., 220-222, 50 (1995).

12) J. F. Drake, Phys. Fluids, 30, 2429 (1987).

13) E. N. Parker, Astrophys. J., 117, 431 (1953).

14) G. B. Field, Astrophys. J., 142, 531 (1965).

15) J. F. Drake, Phys. Fluids, 30, 2429 (1987).

16) S. *R.* Choudhury and P. K. Kaw, Phys. Fluids B, 1, 1646 (1989).

17) S. Deshpande, Phys. Plasmas, 1, 127 (1994).

18) T.W. Petrie, et. al., Nucl. Fusion, vol 37, no. 3, pp 321-338 (1997).

19) W.M. Stacey, M.A. Mahdavi, et. al., Phys. Plasmas, vol 6, no 10, pp 3941-3954 (1999).

20) W. Suttrop, V. Mertens, H. Murmann, et al., "Operational limits for high edge density H-mode tokamak operation", J. Nucl. Mater., 266-269, 118 (1999).

21) A. Loarte, et. al., Nucl. Fusion, vol 38, no. 3, pp 331-371 (1998).

22) N. Hosogane, K. Itami, N. Asakura, et al, J. Nucl. Mater., 220-222, 420 (1995).

23) W.M. Stacey, Phys. Plasmas, vol 6, no 6, pp 2452-2461 (1999).

24) W.M. Stacey, Phys. Plasmas, vol 9, no. 7, pp 3082-3088 (2002).

25) J.J. Martinell, J.A. Almaguer, and J.E.E. Herrera, Plasma Physics. Controlled Fusion 34, 977 (1992).

26) W.M. Stacey, Phys. Plasmas, 6, 2452 (1999).

27) W.M. Stacey, Phys. Plasmas, 11, 686 (2004).

28) W.M. Stacey, T.W. Petrie, Phys. Plasmas, 10, 3949 (2003).

29) General Atomics Fusion Group, http://fusioned.gat.com/fusion_photo_library/Images/d3dtokamak.jpg (2005)

30) General Atomics Fusion Group, http://fusioned.gat.com/fusion_photo_library/viewgraphs.html (2005)

31) General Atomics Fusion Group, http://fusion.gat.com/diag/probes/divlp.html (2005)

32) General Atomics Fusion Group, http://fusion.gat.com/diag/thomson/divertor_thomson.html (2005)

33) General Atomics Fusion Group, http://fusion.gat.com/diag/bolo/ (2005)

34) General Atomics Fusion Group, http://fusion.gat.com/diag/halpha/filterscope.html (2005)

35) W. M. Stacey, T. W. Petrie, Phys. Plasmas, 10, 3949-3952 (2003).

36) P.N. Yushmanov, T. Takizuka, K.S. Reidel et al, Nucl. Fusion 30, 1999 (1990).

37) R. Maingi, M. A. Mahdavi, T. Jernigan *et al.*, Phys. Plasmas 4, 1752 (1997).

38) W.M. Stacey, Nucl. Fusion, vol. 40, pp. 965-973 (2000).

39) W.M. Stacey, Phys. Plasmas, vol 5, no 4, pp 1015-1026 (1998).

40) W. M. Stacey, Phys. Plasmas, vol 8, no 8, pp 3680 (2001).

41) W. M. Stacey, Phys. Plasmas, vol. 3, pp. 2673 (1996).

42) A. DePloey, R. Van der Linden, G. Huysmanns *et al.*, Plasma Phys. Control. Fusion, vol. 39, 423 (1997).

43) W. M. Stacey, Phys. Plasmas, vol. 9, pp. 2692-2706 (2002).